

Semi-Supervised Domain Adaptation with Latent Diffusion for Pathology Image Classification

Tengyue Zhang, Ruiwen Ding, Luoting Zhuang, Yuxiao Wu, Erika F. Rodriguez, William Hsu, *Senior Member, IEEE*

Abstract—Deep learning models in computational pathology often fail to generalize across cohorts and institutions due to domain shift. Existing approaches either fail to leverage unlabeled data from the target domain or rely on image-to-image translation, which can distort tissue structures and compromise model accuracy. In this work, we propose a semi-supervised domain adaptation (SSDA) framework that utilizes a latent diffusion model trained on unlabeled data from both the source and target domains to generate morphology-preserving and target-aware synthetic images. By conditioning the diffusion model on foundation model features, cohort identity, and tissue preparation method, we preserve tissue structure in the source domain while introducing target-domain appearance characteristics. The target-aware synthetic images, combined with real, labeled images from the source cohort, are subsequently used to train a downstream classifier, which is then tested on the target cohort. The effectiveness of the proposed SSDA framework is demonstrated on the task of lung adenocarcinoma prognostication. The proposed augmentation yielded substantially better performance on the held-out test set from the target cohort, without degrading source-cohort performance. The approach improved the weighted F1 score on the target-cohort held-out test set from 0.611 to 0.706 and the macro F1 score from 0.641 to 0.716. Our results demonstrate that target-aware diffusion-based synthetic data augmentation provides a promising and effective approach for improving domain generalization in computational pathology.

Index Terms—Computational pathology, Data augmentation, Diffusion models, Domain adaptation, Image classification

I. INTRODUCTION

DEEP learning (DL) models for computational pathology often exhibit limited generalizability across institutions due to domain shift arising from variations in staining protocols, scanner hardware, and tissue preparation method [1], [2].

This work was supported in part by NIH/National Cancer Institute U2CCA271898, U01CA233370, and the V Foundation. (Corresponding author: William Hsu; e-mail: whsu@mednet.ucla.edu.)

T. Zhang, R. Ding, L. Zhuang, and W. Hsu are with Medical & Imaging Informatics, Department of Radiological Sciences, David Geffen School of Medicine, University of California, Los Angeles (UCLA), Los Angeles, CA 90024, USA. (e-mail: olivia.zhang@ucla.edu; dingrw@ucla.edu; luotingzhuang@g.ucla.edu; whsu@mednet.ucla.edu).

Y. Wu is with the Bioengineering Department, Henry Samueli School of Engineering, UCLA, Los Angeles, CA 90024, USA (e-mail: yuxi.indowu@mednet.ucla.edu).

E. F. Rodriguez is with the Department of Pathology & Laboratory Sciences, David Geffen School of Medicine, UCLA, Los Angeles, CA 90024, USA (e-mail: erikarodriguez@mednet.ucla.edu).

As a result, DL models that demonstrate strong performance during internal validation often have degraded performance when they are tested on external cohorts [3], [4]. This limited generalizability hinders the clinical deployment of DL models in pathology.

Several approaches have been proposed to address domain shift in computational pathology. Classical stain normalization approaches (e.g., Macenko [5], Vahadane [6]) match the source and target color distributions by estimating stain vectors and mapping the stain concentrations of the source image to those of a reference image. A major limitation of these methods is their reliance on a single reference image for normalization; the choice of reference can substantially affect the appearance of normalized images, resulting in poor reproducibility across cohorts. Stain augmentation avoids the reliance on a single image by applying random perturbations to the stain vectors during training to improve robustness [2]. However, these perturbations are not guided by information from the target domain, making these approaches suboptimal when such information is available. Finally, GAN-based stain-transfer and style-transfer methods learn to map source images to the style of the target domain, thereby achieving color normalization [7]–[10]. Yet, they can distort or hallucinate tissue morphology, thereby degrading model accuracy [11], [12].

Effective domain generalization requires leveraging target-domain image appearance information, and modifying target images at test time can distort tissue structure and compromise model performance. This motivates adaptation approaches that can utilize unlabeled data from the target domain during training and do not alter target images at test time. Computational pathology is particularly challenging, as annotations are often difficult or costly to obtain, so target-domain data often do not have readily available labels. Formally, this problem aligns with the semi-supervised domain adaptation (SSDA) problem, where we have: (1) labeled data and unlabeled data from the source domain, (2) unlabeled data from the target domain, and (3) no target images modified at test time. Existing SSDA methods in computational pathology focus on learning stain-invariant [13], [14] or domain-invariant [15], [16] features. Yet, these approaches encourage the learned representations to reduce domain-specific information, which can eliminate biologically meaningful variations across domains.

Diffusion models have demonstrated a strong ability to generate realistic pathology images [17]–[20]. Diffusion models can generate synthetic pathology images with variations from

the real source images while preserving the morphology and semantics of the source images, making them suitable for data augmentation. However, these works primarily evaluate the quality of the diffusion-generated synthetic images or their ability to perform in-domain augmentation. To the best of our knowledge, [21] and [22] are the only works that use diffusion models for domain adaptation; however, they require labeled data from the target domain. No prior study uses a diffusion model to incorporate information from unlabeled target-domain data for improved cross-cohort generalization.

In this work, we propose an SSDA framework in which a latent diffusion model (LDM) is trained on unlabeled data from both the source and target domains and used to generate synthetic images, thereby improving the downstream model's generalization to the target domain. Leveraging the ability of diffusion models to generate diverse images, we create structural variations while preserving the underlying tissue morphology. At the same time, by training the LDM on both domains, we shape a target-aware diffusion prior that captures target-domain appearance (e.g., staining, color, scanner-related differences, tissue preparation-related differences such as tissue thickness), allowing the synthetic images to resemble the target-domain appearances. The LDM is conditioned on feature embeddings extracted from the real source images to preserve tissue morphology, enabling the generation of labeled synthetic images using an LDM trained on unlabeled data. The LDM-generated synthetic images are combined with labeled images from the source domain to train a downstream classifier. We hypothesize that the downstream classifier trained on real source-domain images augmented with the target-aware synthetic images will have better generalization to the target domain, outperforming conventional augmentation methods.

Our contributions are as follows:

- We introduce a novel diffusion-based SSDA framework that leverages unlabeled source- and target-domain images to generate target-aware synthetic data.
- We design a pathology-specific conditioning mechanism that incorporates image embeddings, cohort, and tissue preparation to generate morphology-preserving and target-aware synthetic images.
- We demonstrate the effectiveness of the LDM-based augmentation approach on the lung adenocarcinoma prognosis classification task, showing improvements in the generalization of the downstream model while maintaining the performance of the source cohort.

II. METHODS

A. Overview

1) **Problem formulation:** In the SSDA problem formulation, we have: (1) $\mathcal{D}_s^{\text{unlabeled}} = \{x_j\}$, the unlabeled data from the source domain; (2) $\mathcal{D}_s^{\text{labeled}} = \{(x_i, y_i)\}$, the labeled data from the source domain; (3) $\mathcal{D}_t^{\text{unlabeled}} = \{x_k\}$, the unlabeled data in the target domain. The objective is to use data from the source domain (i.e., $\mathcal{D}_s^{\text{unlabeled}}$ and $\mathcal{D}_s^{\text{labeled}}$) and information about the target domain provided by $\mathcal{D}_t^{\text{unlabeled}}$ to build a classifier that generalizes well to the target domain.

2) **Framework overview:** The overview of our approach is shown in Fig. 1, consisting of three steps. First, an LDM is trained on $\mathcal{D}_s^{\text{unlabeled}}$ and $\mathcal{D}_t^{\text{unlabeled}}$, letting the model learn a generative prior that captures the tissue appearance in the target domain. Second, the LDM is used to generate synthetic source images in a target-aware manner. For each image in $\mathcal{D}_s^{\text{labeled}}$, a synthetic counterpart is generated by conditioning the LDM on a feature embedding extracted from the real source image. Since the LDM is trained on unlabeled images from both domains, the synthetic counterparts may include the appearance characteristics of the target domain. Third, a classifier is trained on real labeled source images combined with target-aware synthetic images. Because the synthetic images include the image appearance of the target domain, the classifier becomes more generalizable to the target domain.

B. Latent diffusion model

1) **LDM architecture:** The LDM consists of a variational autoencoder (VAE), a U-Net denoiser, and a conditioning branch [23]. The VAE encoder converts an input image to a latent space, and the VAE decoder reconstructs the image from the latent representations. The U-Net denoiser performs the reverse diffusion process in the latent space. It predicts the noise added to the latents given a diffusion timestep and the conditions. This setup enables a more efficient diffusion process in the latent space compared to the image space.

In the conditioning branch, we condition the model on three types of information to preserve tissue morphology and incorporate domain-specific variations. For each tile, we obtain: (1) a feature embedding extracted from UNI, a pathology image foundation model [24]; (2) cohort; and (3) tissue-preparation method, i.e., formalin-fixed paraffin-embedded (FFPE) or frozen tissue. The cohort and tissue preparation conditions are one-hot encoded (e.g., 0 = FFPE, 1 = frozen) and then converted into continuous values through embedding layers. Each of these three condition embeddings is passed through a linear layer and concatenated to form the final condition vector. The condition vector is injected into the U-Net via cross-attention layers. The latent representations produced by the U-Net serve as queries, and the condition vector provides keys and values, enabling the image features to learn to attend to the information in the condition vector. Through this cross-attention mechanism, the U-Net denoiser is guided by image-level and cohort-level contexts provided by the conditioning information.

2) **Training the LDM:** The LDM is trained on unlabeled source and target images, i.e., $\mathcal{D}_s^{\text{unlabeled}} \cup \mathcal{D}_t^{\text{unlabeled}}$. We follow the standard denoising diffusion probabilistic model training setup [23]. For a training image x , we obtain the latent representation z from the VAE encoder and perturb z with Gaussian noise to obtain z_t , the noisy latent at diffusion timestep t . The U-Net denoiser is trained to predict the injected noise ϵ and is optimized by the diffusion loss:

$$L_{\text{diff}} = \mathbb{E}_{z, \epsilon, t} [\|\epsilon - \epsilon_{\theta}(z_t, t, c)\|^2] \quad (1)$$

where c is the conditions, t is the diffusion timestep, and $\epsilon_{\theta}(z_t, t, c)$ is the U-Net denoiser's prediction.

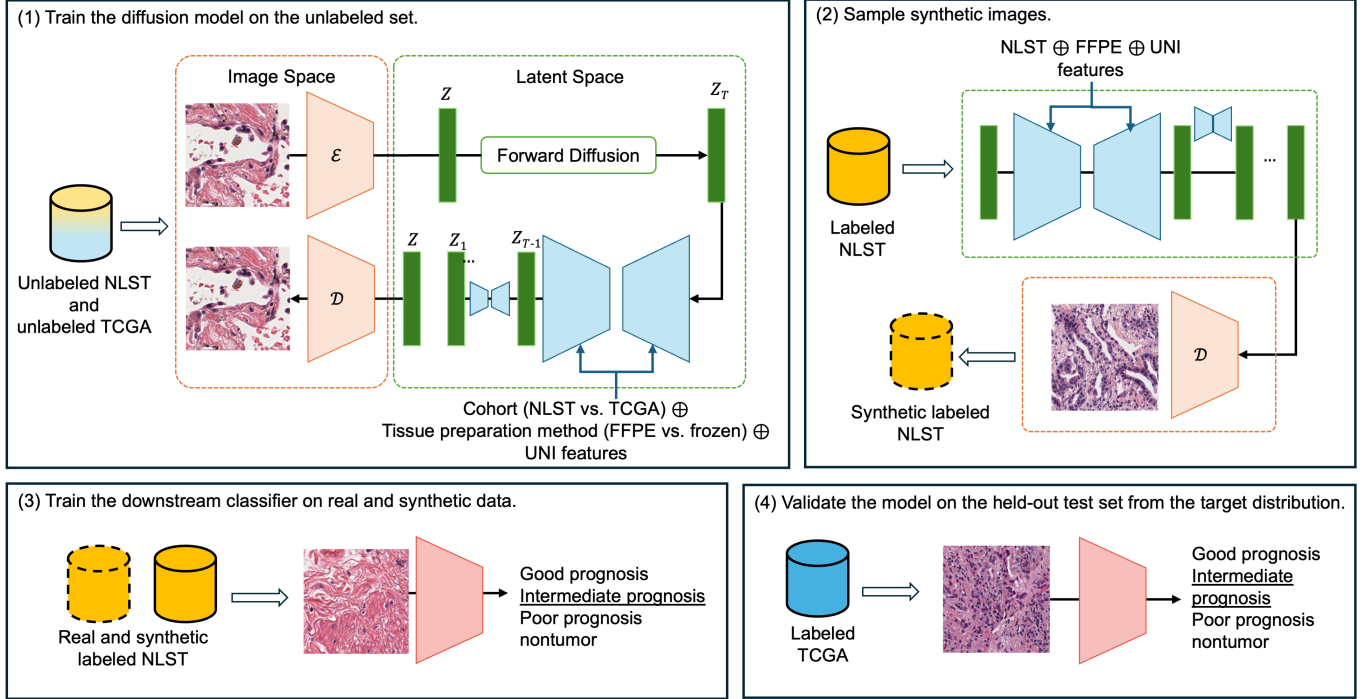


Fig. 1. Overview of the proposed synthetic-augmentation semi-supervised domain adaptation pipeline. The latent diffusion model (LDM) is trained on unlabeled source-domain images (e.g., NLST) and unlabeled target-domain images (e.g., TCGA). Synthetic images are generated from the UNI features of the real, labeled images from NLST. These synthetic NLST tiles are combined with real labeled NLST tiles to train a downstream classifier. The downstream classifier is evaluated on a held-out set of labeled TCGA images, which does not contain patients used for LDM training.

C. Generate synthetic images from the LDM

To generate synthetic images useful for downstream classification, we create a synthetic counterpart for each real, labeled image in the source domain. For each image in $\mathcal{D}_s^{\text{labeled}}$, UNI features were extracted and used to condition the LDM. Because the UNI features used for conditioning encode morphology in the source image, we assume that the synthetic counterpart preserves the same LUAD subtype label as the original image. In this way, we can generate synthetic labeled images from an LDM trained on unlabeled images. Synthetic images are generated via the reverse diffusion process in the latent space, and the latent representation is decoded back into the image space using the VAE decoder.

D. Combining synthetic images with stain augmentation

We further augment the synthetic images generated by the LDM using traditional stain augmentation approaches, namely Macenko stain augmentation [5], [25] and Vahadane stain augmentation [6], [25]. These stain augmentation approaches work by performing stain separation, applying perturbations to the stain vectors, and reconstructing the image from the perturbed stain vectors. Macenko and Vahadane augmentations differ in the way they perform stain separation. Macenko uses Singular Value Decomposition to convert an image into an optical density space, whereas Vahadane uses sparse nonnegative matrix factorization to extract stain components. After generating the synthetic images, we apply these stain augmentation methods to both real and synthetic images when training the

downstream classifier. We use this combined strategy to expose the downstream model to the image appearance and tissue structure learned by the LDM while also introducing more aggressive variability in color and staining through traditional stain augmentation.

E. Downstream classification task & model

1) *Downstream classification task:* We investigate the SSDA problem through the lung adenocarcinoma (LUAD) prognosis classification task, where each pathology image is classified as ‘good prognosis’, ‘intermediate prognosis’, ‘poor prognosis’, or ‘nontumor’. This classification is based on the International Association for the Study of Lung Cancer (IASLC) pathology committee [26]. The ‘good prognosis’ class contains tumors with the lepidic growth pattern. Patients with lepidic-predominant tumors have a 5-year survival of 93%. The ‘intermediate class’ contains tumors with acinar and papillary patterns. Patients with acinar- and papillary-predominant patterns have 5-year survival of 71% and 68%, respectively. Solid and micropapillary patterns are considered to have a poor prognosis, with 5-year survival rates of 39% and 38% [27]. Classifying into these categories is clinically significant as patients with a worse prognosis are more likely to benefit from adjuvant chemotherapy [26]. Similar to other pathology tasks, LUAD prognosis classification is also susceptible to domain shifts [28].

2) *Downstream classification model:* The downstream classification model is trained on the real labeled tiles $\mathcal{D}_s^{\text{labeled}}$

Cohort	# patients	# WSIs	# females	# stage I	Mean age
NLST	190	536	89 (46.8%)	155 (81.6%)	63.7
TCGA	399	1023	216 (54.1%)	275 (68.9%)	65.8

TABLE I
SUMMARY STATISTICS FOR PATIENT CHARACTERISTICS.

augmented by the LDM-generated target-aware synthetic tiles. For each synthetic tile, we assign the same label as its corresponding source tile. The classifier is trained by fine-tuning the Vision Transformer (ViT) architecture [29]. The ViT outputs a probability corresponding to each LUAD subtype and classifies an image into the class with the highest probability. A cross-entropy loss is used to supervise training. When using the synthetic images, we balance the influence of synthetic data on model training by weighting the contributions of the loss terms computed on real and synthetic images. The total loss is:

$$L_{\text{downstream}} = w_s \cdot L_{\text{CE}}^s + (1 - w_s) \cdot L_{\text{CE}}^r \quad (2)$$

where L_{CE}^s and L_{CE}^r denote the cross-entropy loss computed on synthetic and real images, respectively. w_s is found via a grid search.

III. EXPERIMENTS

A. Data

1) **Datasets:** Hematoxylin and Eosin (H&E)-stained whole-slide images (WSIs) were obtained from two publicly available datasets: NLST [30] (190 patients, 536 WSIs) and TCGA [31] (399 patients, 1,023 WSIs). For both datasets, patients were selected such that they had Stage I or Stage II LUAD and at least one WSI available. Characteristics of the patient cohorts are shown in Table I. In our experiments, NLST is treated as the source domain, and TCGA is treated as the target domain.

2) **Data preprocessing:** WSIs are tiled into patches using TRIDENT [32], [33]. Tissue segmentation and penmark removal were first performed on WSIs, and the remaining tissue was tiled into non-overlapping patches. For WSIs scanned at $40\times$ objective magnification, tiles were extracted at $10\times$ magnification with size 512×512 . For WSIs scanned at $20\times$ objective magnification, tiles were extracted at $20\times$ magnification with size 1024×1024 so that the physical area covered by each tile is consistent across WSIs with different objective magnification.

3) **Data splits:** The number of tiles for LDM and downstream classification is shown in Table II. To prevent data leakage, there is no overlap in patient cases with unlabeled tiles used for LDM development and the cases with labeled tiles used for downstream model development or testing. This setup simulates the SSDA setting where domain adaptation is performed on unlabeled data from the target domain, and the downstream classifier is tested on previously unseen patients.

Patients with unlabeled data from NLST and TCGA were split into 80% training and 20% validation, with no overlapping patient cases between the two sets. Tiles from 80% of

patients are used for training the LDM, and the fidelity of the synthetic images is compared against the tiles from the 20% validation patients.

For the downstream classification task, we used 2,638 labeled tiles from NLST for cross-validation and 871 labeled tiles from TCGA for testing. To provide a robust evaluation of model performance, we used 5-fold cross-validation with a patient-level split. In each fold, 20% of patients from NLST were randomly selected as the test set. A multilabel stratified splitting was used to approximately preserve the class distribution across folds. The tiles from the remaining 80% of NLST patients were split into 80% training and 20% validation at the image level. Each model is trained and evaluated across all five folds, and performance is reported on both the cross-validation test sets (NLST) and the held-out test set from TCGA.

B. Baselines and ablation studies

We evaluate our approach by comparing it with standard image and stain augmentation baselines, as well as a baseline using a foundation model. The models compared are:

- 1) **No augmentation:** The model is trained on the training images without applying any data augmentation.
- 2) **Geometric transformations:** Geometric transformations, including random flips and rotations, were applied during training.
- 3) **Color jittering:** Perturbations in brightness, contrast, hues, and saturation were applied to the training images to simulate variations in color.
- 4) **Standard augmentation:** Both geometric transformations and color jittering were applied.
- 5) **Macenko stain augmentation** [5], [25]: Macenko stain augmentation first decomposes the H&E-stained image into H stain and E stain, applies perturbations to the stain concentrations, and reconstructs the image.
- 6) **Vahadane stain augmentation** [6], [25]: Vahadane augmentation follows the same process as Macenko, except that it uses sparse non-negative matrix factorization to separate the H and E stains, which results in more accurate stain separation.
- 7) **UNI + logistic regression (foundation model baseline):** In addition to the data augmentation baselines, we also include a foundation-model baseline to assess whether representations learned by pre-trained pathology foundation models can mitigate cross-cohort domain shifts. In this model, tile-level features are extracted from UNI [24]. Following the linear probing approach suggested by the authors, we fit a multinomial logistic regression model on NLST features and evaluate it on the held-out test set from TCGA.
- 8) **LDM synthetic augmentation (proposed):** This model uses synthetic images generated by the LDM to augment the training data.
- 9) **LDM synthetic + Macenko (proposed):** This model applies Macenko stain augmentation to the real and LDM-generated synthetic images during training as described in Sec. II-D.

Cohort	Diffusion (unlabeled)		Downstream (labeled)		
	Train	Validation	Train	Validation	Test
NLST	1,256,490	311,355	1716	429	493
TCGA	1,215,329	275,820	0	0	871
Total	2,471,819	587,175	1716	429	493 from the CV test set 871 from the held-out test set

TABLE II

NUMBER OF TILES USED FOR DIFFUSION MODEL TRAINING/VALIDATION AND DOWNSTREAM CLASSIFIER TRAINING/VALIDATION/TESTING. THERE ARE NO OVERLAPPING PATIENT CASES BETWEEN THE UNLABELED SET FOR DIFFUSION DEVELOPMENT AND THE LABELED SET FOR DOWNSTREAM TO SIMULATE THE SEMI-SUPERVISED DOMAIN ADAPTATION SETTING.

	Good prognosis	Intermediate prognosis	Poor prognosis	Non-tumor	Total
NLST	456 (17.29%)	910 (34.50%)	720 (27.29%)	552 (20.92%)	2,638 (100%)
TCGA	114 (13.09%)	271 (31.11%)	271 (31.11%)	215 (24.68%)	871 (100%)

TABLE III

NUMBER OF TILES OF EACH LUNG ADENOCARCINOMA PROGNOSTIC CATEGORY IN THE DOWNSTREAM LABELED SET.

10) **LDM synthetic + Vahadane (proposed):** This model applies Vahadane stain augmentation to the real and LDM-generated synthetic images during training as described in Sec. II-D.

In addition to the baselines, we also conducted ablation studies to examine the effect of LDM training data on the generalization of the downstream model. Specifically, we compared models trained using synthetic images generated by an LDM trained on NLST+TCGA with those trained on NLST only.

C. Model evaluation

1) *Evaluating the LDM:* To evaluate the quality and fidelity of LDM-generated synthetic images, the Fréchet Inception Distance (FID) of the Inception-V3 features [34] was computed on the validation split of unlabeled data. FID measures the similarity of the distributions of real and synthetic images. It assumes each set of features follows a multidimensional Gaussian distribution and computes the Fréchet distance between two sets of features. To calculate FID, we randomly selected 10,000 images from the validation split of the unlabeled data, maintaining the same proportion of NLST and TCGA cases as in the full validation split. For each selected image, UNI features, cohort, and tissue preparation information were extracted and used to generate a synthetic counterpart using the LDM. Finally, FID was calculated on the 10,000 real validation images and the 10,000 condition-matched synthetic images.

2) *Evaluating downstream classifiers:* F1 score was used to measure the performance of downstream models. We used the F1 score because LUAD prognosis classification is class-imbalanced, making accuracy a misleading metric. Moreover, the F1 score balances false positives and false negatives, consistent with the clinical setting, where both have critical consequences. In addition to per-class F1 scores, macro F1 (i.e., unweighted average) and weighted F1 (i.e., weighted by number of instances in each class) were calculated to provide an overall measure of model performance. 5-fold

cross-validation F1 scores were compared between models using a paired *t*-test, where $p < 0.05$ was considered to be statistically significant.

D. Implementation details

1) *LDM:* We implemented the LDM using the PathLDM framework [19] and initialized the pre-trained VAE of PathLDM. The VAE is a Vector-Quantized Variational Autoencoder (VQ-VAE) with three latent channels and a down-sampling factor of 4. The diffusion model follows a standard latent diffusion formulation, with 1,000 diffusion steps and a linear noise schedule. The U-Net denoiser was trained from scratch for 150,000 iterations, optimized using AdamW with a base learning rate of 5×10^{-5} and cosine decay. Classifier-free guidance was used. The conditioning information was dropped with a probability of 0.1 during training. During inference, the classifier-free guidance scale was set to 1.5. Images were resized to 256×256 pixels. An effective batch size of 48 was used, with 24 samples per GPU and 2 GPUs. All training and inference were performed on NVIDIA L40S GPUs.

2) *Downstream classifiers:* For the downstream classification task, we fine-tuned an ImageNet [35] pre-trained ViT-B/16 model [29] from Hugging Face [36]. Images were resized to 224×224 and normalized by the mean and standard deviation of ImageNet statistics. Models were trained with the Adam optimizer [37], learning rate 1×10^{-4} , weight decay 1×10^{-4} , and batch size 32. All models were trained for a maximum of 200 epochs, with an early stopping patience of 5, monitored by the validation loss. All downstream experiments were done on a single NVIDIA L40S GPU.

IV. RESULTS

A. LDM-generated synthetic images

We evaluated the LDM using 10,000 real validation images and 10,000 synthetic images. The LDM achieved an FID of 5.779. In practice, FID values below 10 are generally considered indicative of high fidelity. Our FID value reveals a

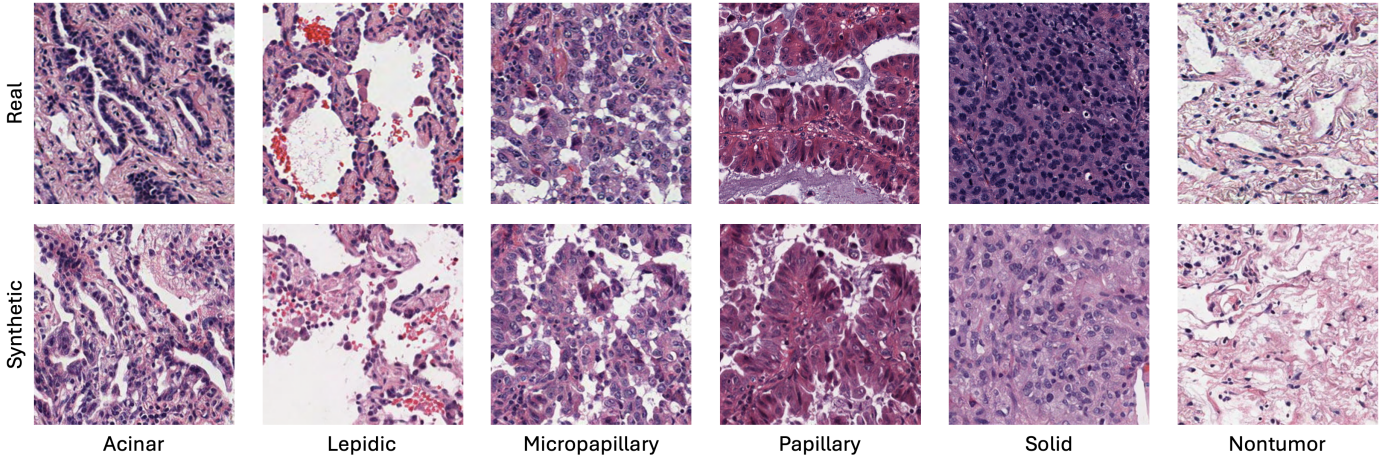


Fig. 2. Examples of real and synthetic NLST images. For each real NLST image in the top row, a corresponding synthetic tile (bottom row) was generated from the LDM. The synthetic images preserve morphology while introducing variations in image appearance and tissue structures. Additional examples are provided in Supplementary Fig. S1.

strong similarity between the real and synthetic image distributions, suggesting that the LDM generates high-fidelity images that accurately capture the characteristics of LUAD pathology images. Representative examples are shown in Fig. 2.

B. Synthetic images enable target-aware augmentation

To assess whether the synthetic images generated by the LDM can capture the image appearance of the target cohort, we performed t-SNE projections of embeddings from CONCH, a vision-language histopathology foundation model [38], to compare the feature distribution of real and synthetic images. Since UNI embeddings were used for conditioning, t-SNE projections of the UNI embeddings are expected and, in fact, show substantial overlap between real and synthetic images. This overlap shows the LDM preserves information in the UNI features but is not informative for assessing the additional variations provided by the LDM. Therefore, we used CONCH embeddings to visualize the domain gap bridged by the LDM-generated synthetic data. 800 unlabeled NLST and 800 unlabeled TCGA tiles were selected from the validation set, and synthetic counterparts of the 800 NLST images were generated using the LDM. As shown in Fig. 3(a), while the two cohorts do not exhibit completely separated clusters, there is a noticeable gap between the feature space of NLST images and that of TCGA images in certain areas, as indicated by the red circle. Fig. 3(b) shows the t-SNE projection after adding synthetic NLST images. The synthetic images fill the gaps between the original NLST and TCGA feature spaces, interpolating the two distributions. This indicates that the synthetic tiles capture characteristics more similar to the TCGA cohort compared to the original real NLST tiles.

C. Downstream classification performance

1) *Held-out test set from the target cohort*: To assess whether the downstream classifiers generalize to the target cohort, we evaluated all models on the held-out labeled TCGA test set,

which consists entirely of patients unseen in LDM training and evaluation. All three variants of the LDM-based augmentation models improved the generalization to TCGA, indicating the effectiveness of diffusion-based data augmentation. The model using LDM+Vahadane augmentations achieved the best overall F1 scores (weighted 0.706, macro 0.716) and the best F1 scores on the ‘intermediate prognosis’ (0.710) and ‘poor prognosis’ (0.592) classes. LDM synthetic augmentation achieved the best F1 scores in the ‘good prognosis’ (0.769) and ‘nontumor’ (0.835) classes while achieving the second-best macro F1 (0.701).

In the baseline models, geometric transformation and Macenko stain augmentation yielded moderate improvements in model performance on the TCGA held-out test set, resulting in higher overall F1 scores compared to the model with no augmentation. Among all baseline models, Vahadane augmentation showed the largest improvement over the no-augmentation model, achieving a weighted F1 score of 0.647; however, the differences were not statistically significant ($p > 0.5$). Color jittering and standard augmentation worsened model performance on TCGA, resulting in lower overall F1 scores compared to the no-augmentation model. Notably, the logistic regression model using foundation model features did not outperform fine-tuned ViT when stain and/or LDM-based augmentation were used. This indicates that, although UNI offers robust general-purpose representations, when the features are fine-tuned for specific tasks, they are insufficient in overcoming cross-domain and cross-cohort differences.

Comparing the proposed LDM-based approaches with baseline methods, all three LDM-based models substantially improved the generalization to TCGA compared to the no-augmentation model. As shown in Fig. 4, the LDM+Vahadane model yielded significantly better F1 scores than all baseline models in the ‘poor prognosis’ and ‘intermediate prognosis’ classes, as well as weighted and macro F1 scores. It also improved the nontumor class, significantly outperforming color jittering, geometric transformation, and Vahadane augmentation. Combining LDM-based augmentation with Macenko

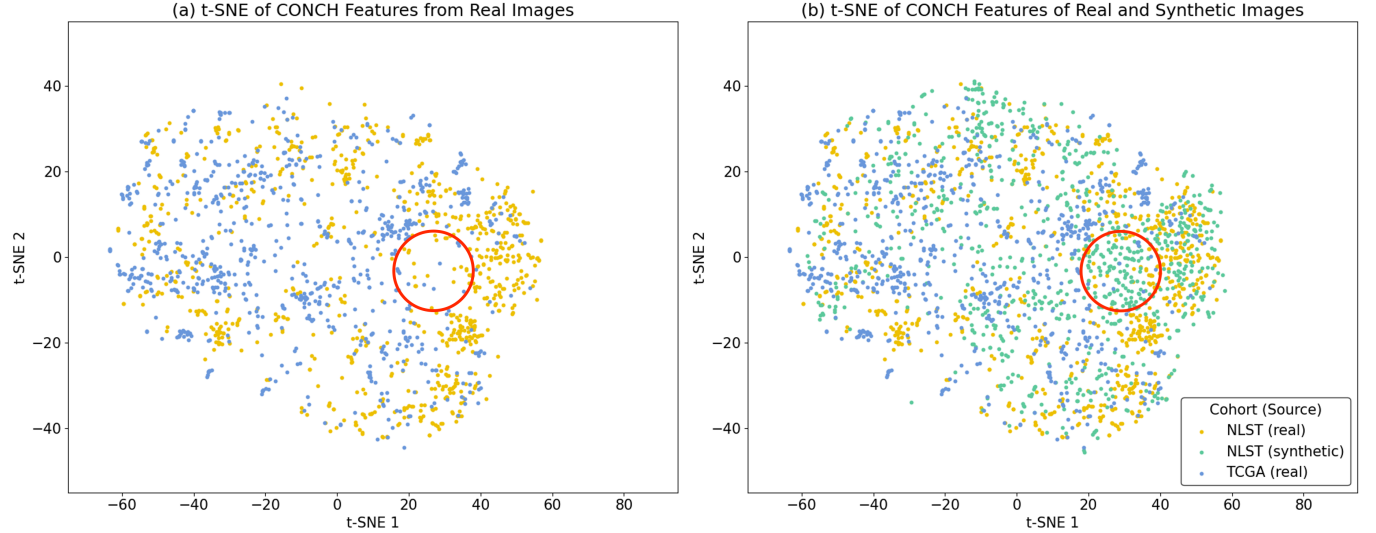


Fig. 3. t-SNE visualization of real NLST, real TCGA, and synthetic NLST tiles. Plots are generated using CONCH feature embeddings. (a) shows the t-SNE feature space of real NLST and real TCGA tiles. (b) shows the t-SNE with real NLST, real TCGA, and synthetic NLST tiles. While real NLST and real TCGA images do not exhibit completely separated clusters, there still exist gaps between the two domains, as highlighted by the red circle. Synthetic NLST tiles generated by the LDM occupies an intermediate space between NLST and TCGA distributions, indicating that using unlabeled TCGA during diffusion training influences the generative prior and introduces target-domain characteristics.

augmentation also improved model performance on the held-out test set. The LDM+Macenko model significantly outperformed the Macenko-only model, achieving higher weighted and macro F1 scores ($p < 0.01$). Notably, across all models, differences in model performance in TCGA on the ‘good prognosis’ class were not statistically significant between any pair of models.

2) Cross-validation on the source cohort: We also evaluated model performance on the source domain. Table V summarizes the mean and standard deviation of per-class and overall F1 scores on the cross-validation test sets from NLST. Among all models, the standard, LDM+Macenko, and LDM+Vahadane augmentations improved the macro F1 scores marginally, with no statistically significant difference. The LDM synthetic augmentation yielded slightly lower F1 scores; however, the differences were not significant in overall F1 scores or the per-class F1 scores, except for the ‘intermediate prognosis’ class ($p = 0.02$). Overall, LDM-based augmentation improves generalization to the target cohort without sacrificing performance on the source cohort.

D. Per-class domain shift analysis

As shown in Sec. IV-C, all data augmentation methods had similar performance on the ‘good prognosis’ class, which consists of tiles with the lepidic growth pattern. To investigate the class-level performance differences, we performed t-SNE analysis of CONCH [38] feature embeddings of the ‘good prognosis’ tiles from NLST and TCGA. As shown in Fig. 5, the ‘good prognosis’ tiles from the two cohorts showed substantial overlap, unlike the significant cross-cohort separation observed in Fig. 3. This suggests that the class-level domain shift in the ‘good prognosis’ class is less significant compared to the overall cohort-level domain shift, limiting the potential

gain in domain generalization from data augmentation. This observation also aligns with the biological characteristics of the lepidic growth pattern. Lepidic tiles usually exhibit the growth of tumor cells along intact alveolar structures and have minimal stromal or pleural invasions, resulting in a highly distinctive and less varying morphology [26]. These features make the lepidic images less sensitive to cohort-specific variabilities, making it easier for DL models to learn truly meaningful patterns instead of cohort-specific noise.

E. Ablation studies

In our ablation studies, we compared two variants of the LDM to see the effectiveness of using unlabeled data from the target cohort to improve the generalizability of the downstream model. The two LDMs we compared are: (1) an LDM trained only on unlabeled data from NLST, and (2) an LDM trained on unlabeled data from both NLST and TCGA. All other components in the pipeline remain unchanged except for the training data of the LDM. Table VI summarizes model performance on the NLST cross-validation test sets and the TCGA held-out test set.

When we evaluated both models on the NLST cross-validation test sets, there was no statistically significant difference in weighted or macro F1 scores ($p = 0.12$ and $p = 0.09$, respectively). In contrast, on the TCGA held-out test set, the downstream model using synthetic images from the LDM trained on both cohorts achieved substantially higher performance (weighted F1: 0.680 vs. 0.614; macro F1: 0.7011 vs. 0.640), with both being statistically significant. This ablation shows that incorporating unlabeled data from the target cohort during LDM training yields improvements in target-cohort generalization without sacrificing source-cohort performance.

	Good prognosis	Intermediate prognosis	Poor prognosis	Nontumor	Weighted	Macro
UNI + logistic regression	0.597 ± 0.080	0.660 ± 0.030	0.500 ± 0.077	0.739 ± 0.013	0.622 ± 0.029	0.624 ± 0.032
No augmentation	0.754 ± 0.028	0.655 ± 0.021	0.359 ± 0.113	0.797 ± 0.021	0.611 ± 0.046	0.641 ± 0.039
Geometric transformation	0.730 ± 0.064	0.639 ± 0.023	0.411 ± 0.060	0.791 ± 0.039	0.617 ± 0.014	0.643 ± 0.016
Color jittering	0.753 ± 0.043	0.632 ± 0.010	0.293 ± 0.091	0.767 ± 0.030	0.576 ± 0.022	0.611 ± 0.014
Standard augmentation	0.756 ± 0.030	0.639 ± 0.029	0.303 ± 0.134	0.772 ± 0.061	0.583 ± 0.061	0.617 ± 0.052
Macenko stain augmentation	0.760 ± 0.030	0.654 ± 0.012	0.389 ± 0.118	0.801 ± 0.033	0.622 ± 0.032	0.651 ± 0.024
Vahadane stain augmentation	0.726 ± 0.032	0.672 ± 0.027	0.486 ± 0.101	0.775 ± 0.027	0.647 ± 0.042	0.665 ± 0.035
LDM synthetic augmentation (proposed)	0.769 ± 0.028	0.675 ± 0.017	0.526 ± 0.072	0.835 ± 0.019	0.680 ± 0.019	0.701 ± 0.012
LDM synthetic + Macenko stain augmentation (proposed)	0.722 ± 0.027	0.683 ± 0.029	0.546 ± 0.047	0.833 ± 0.036	<u>0.683 ± 0.018</u>	0.696 ± 0.018
LDM synthetic + Vahadane stain augmentation (proposed)	0.731 ± 0.047	0.710 ± 0.021	0.592 ± 0.041	0.830 ± 0.020	0.706 ± 0.025	0.716 ± 0.027

TABLE IV
MEAN F1 SCORE \pm STANDARD DEVIATION FOR EACH CLASS AND AVERAGED METRICS (WEIGHTED AND MACRO) ACROSS DIFFERENT AUGMENTATION STRATEGIES ON THE TARGET COHORT (TCGA).

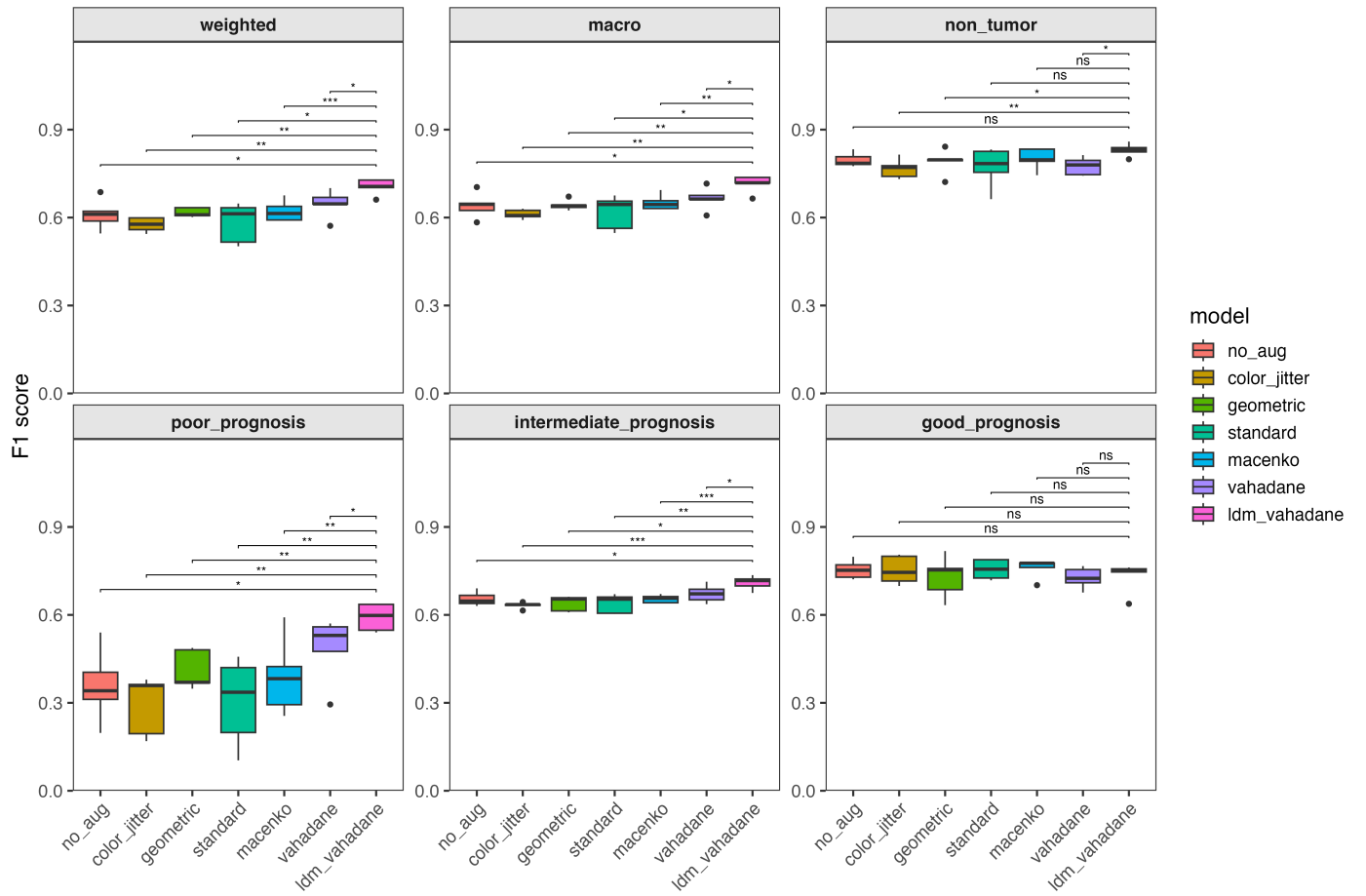


Fig. 4. Box plots showing the distribution of F1 scores from 5-fold cross-validation when model using different data augmentation approaches are tested on the TCGA held-out test set. Statistical significance is represented by * ($p < 0.05$), ** ($p < 0.01$), *** ($p < 0.001$), or ns ($p > 0.05$).

V. DISCUSSION

DL models in computational pathology often struggle to generalize across different domains. Existing domain adaptation approaches either fail to leverage unlabeled data from the target domain or employ image-to-image translation methods, which can distort tissue structure and morphology, thereby degrading model performance. In this work, we present a

semi-supervised domain adaptation framework based on latent diffusion models, which uses unlabeled images from both source and target domains to generate synthetic images in a target-aware manner. Our results show that the LDM-generated synthetic images, by bridging the gap between the two domains, improve the performance of downstream classifiers on the held-out test set from the target cohort without sacrificing

	Good prognosis	Intermediate prognosis	Poor prognosis	Nontumor	Weighted	Macro
UNI + logistic regression	0.702 \pm 0.098	0.664 \pm 0.170	0.686 \pm 0.153	0.662 \pm 0.154	0.711 \pm 0.119	0.678 \pm 0.117
No augmentation	0.675 \pm 0.134	0.721 \pm 0.075	0.694 \pm 0.125	0.837 \pm 0.071	0.763 \pm 0.078	0.732 \pm 0.062
Geometric transformation	0.694 \pm 0.144	0.686 \pm 0.084	0.611 \pm 0.163	0.815 \pm 0.057	0.714 \pm 0.085	0.701 \pm 0.073
Color jittering	0.678 \pm 0.151	0.657 \pm 0.078	0.604 \pm 0.199	0.834 \pm 0.049	0.718 \pm 0.113	0.693 \pm 0.093
Standard augmentation	0.694 \pm 0.095	0.713 \pm 0.103	0.710 \pm 0.138	0.812 \pm 0.068	0.770 \pm 0.072	0.732 \pm 0.056
Macenko stain augmentation	0.718 \pm 0.141	0.735 \pm 0.072	0.640 \pm 0.193	0.796 \pm 0.070	0.758 \pm 0.089	0.722 \pm 0.071
Vahadane stain augmentation	0.754 \pm 0.090	0.710 \pm 0.080	0.688 \pm 0.158	0.765 \pm 0.121	0.761 \pm 0.077	0.729 \pm 0.069
LDM synthetic augmentation (proposed)	0.704 \pm 0.141	0.649 \pm 0.083	0.680 \pm 0.161	0.842 \pm 0.040	0.736 \pm 0.111	0.719 \pm 0.081
LDM synthetic + Macenko stain augmentation (proposed)	0.714 \pm 0.103	<u>0.724 \pm 0.105</u>	0.723 \pm 0.144	0.805 \pm 0.065	0.771 \pm 0.089	0.741 \pm 0.065
LDM synthetic + Vahadane stain augmentation (proposed)	0.711 \pm 0.083	0.716 \pm 0.103	0.698 \pm 0.184	0.811 \pm 0.082	0.760 \pm 0.096	<u>0.734 \pm 0.075</u>

TABLE V

MEAN F1 SCORE \pm STANDARD DEVIATION FOR EACH CLASS AND AVERAGED METRICS (WEIGHTED AND MACRO) ACROSS DIFFERENT AUGMENTATION STRATEGIES ON THE SOURCE COHORT (NLST).

	Good prognosis	Intermediate prognosis	Poor prognosis	Nontumor	Weighted	Macro
Cross-validation test set (NLST)						
NLST	0.743 \pm 0.110	0.716 \pm 0.073	0.662 \pm 0.160	0.824 \pm 0.038	0.761 \pm 0.084	0.736 \pm 0.065
NLST + TCGA	0.704 \pm 0.141	0.649 \pm 0.083	0.680 \pm 0.161	0.842 \pm 0.040	0.736 \pm 0.111	0.719 \pm 0.081
Held-out test set from the target cohort (TCGA)						
NLST	0.719 \pm 0.034	0.657 \pm 0.016	0.364 \pm 0.077	0.818 \pm 0.022	0.614 \pm 0.030	0.640 \pm 0.028
NLST + TCGA	0.769 \pm 0.028	0.675 \pm 0.017	0.526 \pm 0.072	0.835 \pm 0.019	0.680 \pm 0.019	0.701 \pm 0.012

TABLE VI

PER-CLASS AND OVERALL (WEIGHTED AND MACRO) F1 SCORES (MEAN \pm STANDARD DEVIATION) WHEN THE LDM IS TRAINED ON UNLABELED NLST ONLY VS. UNLABELED NLST+TCGA.

performance on the source cohort. Models using synthetic images achieved substantially higher F1 scores compared to baseline augmentation methods.

The LDM-based data augmentation is effective in improving the generalizability of downstream models because it incorporates target-domain appearance while preserving realistic tissue morphology. By training the LDM on unlabeled data from both source and target domains, the LDM learns a generative prior that incorporates the difference between the two domains, including staining, scanners, or site-specific variations. In our conditioning mechanism, by conditioning the LDM on UNI features, we preserved tissue morphology. As a result, when using the LDM to generate target-aware synthetic images, the synthetic images retain the tissue morphology in the source images while exhibiting some characteristics of the target domain. Moreover, by conditioning the LDM on UNI features, we successfully generated synthetic images labeled by LUAD subtype using an LDM trained on unlabeled data. We demonstrated the fidelity of the synthetic images with FID and showed their effectiveness in bridging the domain gap through a t-SNE analysis. Finally, using the synthetic images, we exposed the downstream classifier to morphologically accurate but appearance-augmented examples during training, improving their generalization to the target cohort.

Additionally, we found that stain augmentation complements LDM-based augmentation. This observation is consistent with how the two augmentation approaches create

variabilities. First, although the LDM learned the staining distributions in NLST and TCGA, the synthetic images remain closely tied to the source morphology. This limits the degree of staining variation produced by the LDM: the changes are realistic and target-aware, but not too aggressive to make the resulting image unrealistic. In contrast, stain augmentation applies explicit perturbations to the hematoxylin and eosin stain vectors, enabling a broader range of color and staining variability than the LDM alone. Thus, stain augmentation complements the LDM by expanding variability in staining that the diffusion model produces. Second, the LDM-generated images have slight structural variations compared to the source images. They are morphologically consistent with the original tiles but are not pixel-wise replicas. In contrast, stain augmentation applies perturbations solely to the color and staining of the tiles, without altering the tissue structure. Together, these two augmentation types offer distinct types of variability: LDM provides target-aware appearance and subtle structural variation, while Vahadane offers strong, explicit staining variation. By combining these two, the downstream model is exposed to variabilities in staining, appearance, and tissue structure, resulting in a more effective data augmentation approach.

In our per-class evaluation of downstream models, we found that all augmentation methods generally yielded no significant improvement in the ‘good prognosis’ class and resulted in higher standard deviations in the ‘poor prognosis’

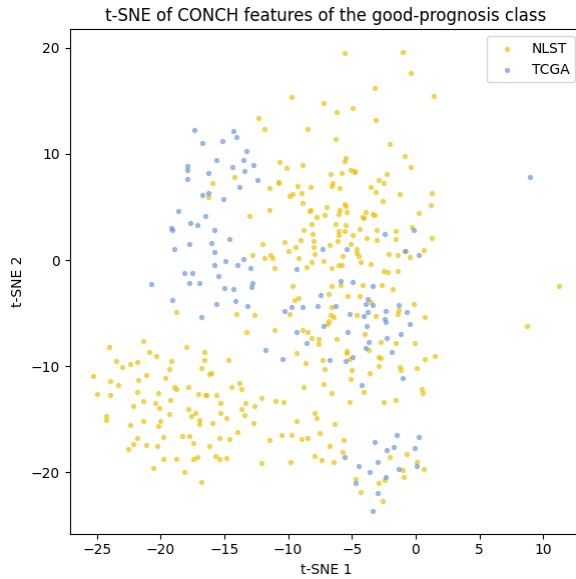


Fig. 5. t-SNE visualization of CONCH feature embeddings for NLST and TCGA tiles in the 'good prognosis' class. A substantial overlap exists between NLST and TCGA data points, indicating a smaller cross-cohort domain shift in this class.

class. For the 'good prognosis' class, which consists of tiles with the lepidic growth pattern, our analysis suggests that the domain shift between NLST and TCGA for this class is smaller compared to the overall domain shift. This finding is consistent with the biological characteristics of the lepidic growth pattern, which refers to tumor cells growing along the alveoli without significant stromal or pleural invasion. This characteristic results in relatively lower variability in image appearance. As a result, data augmentation approaches provide limited additional benefits for this class compared to more heterogeneous classes, such as the 'intermediate prognosis' and 'poor prognosis' classes. For the 'poor prognosis' class, across all models, we observed a higher standard deviation compared to other classes. This class consists of tiles with the solid and micropapillary growth patterns. Since tiles may contain tumors exhibiting both patterns, the tiles are more diverse in their tissue architecture. Additionally, these regions are more often affected by necrosis, inflammation, and desmoplasia compared to the lepidic pattern [26], making it more difficult for DL models to learn consistent features and therefore resulting in higher standard deviations across the five folds.

The ablation studies highlight the significance of using unlabeled data from the target domain during LDM training for effective SSDA. The LDM trained on both NLST and TCGA improved generalization to TCGA, achieving significantly higher weighted and macro F1 scores, whereas the LDM trained on NLST did not. This finding demonstrates that using data from both source and target domains for training allows the LDM to generate synthetic counterparts of source-cohort images that share the characteristics of target-cohort images, therefore improving the downstream classifier's generalization. Moreover, since we generated the same number of synthetic tiles from each LDM variant, the improvement of the proposed approach over the baseline data augmentation is not a result of

merely increased downstream training data volume, but rather the target-aware generation.

Our findings have several implications. First, the proposed approach effectively enhances model generalization to external cohorts, as it improves cross-domain generalization without compromising performance on the source domain. Secondly, the proposed approach does not use labels from the target domain, making it suitable for scenarios such as pathology images, where unlabeled data are often available as annotations are costly or cannot be shared due to privacy concerns.

One limitation of this work is the computational cost. Diffusion models are computationally expensive, both during training and synthetic image generation. Even though we attempted to alleviate this issue by using a latent-space diffusion model instead of an image-space model, the LDM remains computationally costly. In our experiments, training was performed on 2 NVIDIA L40S GPUs, each with 46GB virtual memory, and required approximately 76 hours to complete. Moreover, generating a single synthetic image requires multiple passes through the U-Net denoiser, making it time-consuming to generate large-scale synthetic datasets. These computational requirements limit the usability of diffusion models in environments with limited computational resources. Additionally, while our analysis has shown that LDM-based data augmentation improves generalization, one needs to balance the tradeoff between better generalization and computation. In scenarios where access to the computational resources required for diffusion models is unavailable, stain augmentation, particularly Vahadane, can be a practical alternative.

VI. CONCLUSION

In summary, this work demonstrates that utilizing latent diffusion models for SSDA facilitates improved generalization of pathology classification models to the target domain. By training an LDM on unlabeled images from both the source and target domains, the LDM can generate morphologically accurate and target-aware images. Using both target-aware synthetic images and traditional stain augmentation approaches, the downstream classifier is exposed to variations in tissue structure, image appearance, and staining, thereby achieving better generalization to the target domain. While this work demonstrates the effectiveness of the proposed approach on the LUAD subtype classification task, it can be readily extended to any setting where some unlabeled data from the target domain are available. As part of our future work, we will explore conditioning mechanisms to better preserve details in tissue morphology and reduce noise in the labels of the synthetic data. Overall, this work highlights the utility of diffusion models in enhancing domain adaptation in computational pathology.

CONFLICT OF INTEREST STATEMENT

WH reports receiving research funding from EarlyDiagnostics Inc and consulting fees from the Radiological Society of North America for editorial services. The remaining authors have no conflicts of interest to declare.

REFERENCES

[1] B. Sahiner, W. Chen, R. K. Samala, and N. Petrick, "Data drift in medical machine learning: implications and potential remedies," *The British Journal of Radiology*, vol. 96, no. 1150, p. 20220878, 2023.

[2] M. Jahanifar, M. Raza, K. Xu, T. T. L. Vuong, R. Jewsbury, A. Shephard, N. Zamanitajeddin, J. T. Kwak, S. E. A. Raza, F. Minhas, *et al.*, "Domain generalization in computational pathology: survey and guidelines," *ACM Computing Surveys*, vol. 57, no. 11, pp. 1–37, 2025.

[3] Y. Jiao, J. Li, and S. Fei, "Staining condition visualization in digital histopathological whole-slide images," *Multimedia Tools and Applications*, vol. 81, no. 13, pp. 17831–17847, 2022.

[4] J. Van der Laak, G. Litjens, and F. Ciompi, "Deep learning in histopathology: the path to the clinic," *Nature medicine*, vol. 27, no. 5, pp. 775–784, 2021.

[5] M. Macenko, M. Niethammer, J. S. Marron, D. Borland, J. T. Woosley, X. Guan, C. Schmitt, and N. E. Thomas, "A method for normalizing histology slides for quantitative analysis," in *2009 IEEE international symposium on biomedical imaging: from nano to macro*, pp. 1107–1110, IEEE, 2009.

[6] A. Vahadane, T. Peng, A. Sethi, S. Albarqouni, L. Wang, M. Baust, K. Steiger, A. M. Schlitter, I. Esposito, and N. Navab, "Structure-preserving color normalization and sparse stain separation for histological images," *IEEE transactions on medical imaging*, vol. 35, no. 8, pp. 1962–1971, 2016.

[7] C. Cong, S. Liu, A. Di Ieva, M. Pagnucco, S. Berkovsky, and Y. Song, "Colour adaptive generative networks for stain normalisation of histopathology images," *Medical Image Analysis*, vol. 82, p. 102580, 2022.

[8] L. Jose, S. Liu, C. Russo, A. Nadort, and A. Di Ieva, "Generative adversarial networks in digital pathology and histopathological image processing: a review," *Journal of Pathology Informatics*, vol. 12, no. 1, p. 43, 2021.

[9] H. Kang, D. Luo, W. Feng, S. Zeng, T. Quan, J. Hu, and X. Liu, "Stainnet: a fast and robust stain normalization network," *Frontiers in Medicine*, vol. 8, p. 746307, 2021.

[10] Z. Xu, X. Huang, C. F. Moro, B. Bozóky, and Q. Zhang, "Gan-based virtual re-staining: a promising solution for whole slide image analysis," *arXiv preprint arXiv:1901.04059*, 2019.

[11] Z. Du, P. Zhang, X. Huang, Z. Hu, G. Yang, M. Xi, and D. Liu, "Deeply supervised two stage generative adversarial network for stain normalization," *Scientific Reports*, vol. 15, no. 1, p. 7068, 2025.

[12] V. C. Pezoulas, D. I. Zaridis, E. Mylona, C. Androutsov, K. Apostolidis, N. S. Tachos, and D. I. Fotiadis, "Synthetic data generation methods in healthcare: A review on open-source tools and methods," *Computational and structural biotechnology journal*, vol. 23, pp. 2892–2910, 2024.

[13] S. Otálora, M. Atzori, V. Andreadczyk, A. Khan, and H. Müller, "Staining invariant features for improving generalization of deep convolutional neural networks in computational pathology," *Frontiers in bioengineering and biotechnology*, vol. 7, p. 198, 2019.

[14] N. Marini, M. Atzori, S. Otálora, S. Marchand-Maillet, and H. Müller, "H&e-adversarial network: a convolutional neural network to learn stain-invariant features through hematoxylin & eosin regression," in *Proceedings of the IEEE/CVF International Conference on Computer Vision*, pp. 601–610, 2021.

[15] M. W. Lafarge, J. P. Pluim, K. A. Eppenhof, and M. Veta, "Learning domain-invariant representations of histological images," *Frontiers in medicine*, vol. 6, p. 162, 2019.

[16] K. Fang and G. Ding, "A domain-invariant feature learning framework for histopathology images," in *Third International Conference on Advanced Algorithms and Neural Networks (AANN 2023)*, vol. 12791, pp. 392–397, SPIE, 2023.

[17] S. Yellapragada, A. Graikos, K. Triaridis, P. Prasanna, R. Gupta, J. Saltz, and D. Samaras, "Zoomldm: Latent diffusion model for multi-scale image generation," in *Proceedings of the Computer Vision and Pattern Recognition Conference*, pp. 23453–23463, 2025.

[18] A. Graikos, S. Yellapragada, M.-Q. Le, S. Kapse, P. Prasanna, J. Saltz, and D. Samaras, "Learned representation-guided diffusion models for large-image generation," in *Proceedings of the IEEE/CVF Conference on Computer Vision and Pattern Recognition*, pp. 8532–8542, 2024.

[19] S. Yellapragada, A. Graikos, P. Prasanna, T. Kunc, J. Saltz, and D. Samaras, "Pathldm: Text conditioned latent diffusion model for histopathology," in *Proceedings of the IEEE/CVF Winter Conference on Applications of Computer Vision*, pp. 5182–5191, 2024.

[20] S. Alfasy, W. Uegami, M. E. HOQ, G. Alabtah, and H. Tizhoosh, "Semantic and visual crop-guided diffusion models for heterogeneous tissue synthesis in histopathology," in *The Thirty-ninth Annual Conference on Neural Information Processing Systems*, 2025.

[21] S. C. Gullapally, Y. Zhang, N. K. Mittal, D. Kartik, S. Srinivasan, K. Rose, D. Shenker, D. Juyal, H. Padigela, R. Biju, *et al.*, "Synthetic domain-targeted augmentation (s-dota) improves model generalization in digital pathology," *arXiv preprint arXiv:2305.02401*, 2023.

[22] D. J. Drexlin, J. Dippel, J. Hense, N. Prenišl, G. Montavon, F. Klauschen, and K.-R. Müller, "Medi: Metadata-guided diffusion models for mitigating biases in tumor classification," in *International Conference on Medical Image Computing and Computer-Assisted Intervention*, pp. 379–388, Springer, 2025.

[23] R. Rombach, A. Blattmann, D. Lorenz, P. Esser, and B. Ommer, "High-resolution image synthesis with latent diffusion models," in *Proceedings of the IEEE/CVF conference on computer vision and pattern recognition*, pp. 10684–10695, 2022.

[24] R. J. Chen, T. Ding, M. Y. Lu, D. F. Williamson, G. Jaume, A. H. Song, B. Chen, A. Zhang, D. Shao, M. Shaban, *et al.*, "Towards a general-purpose foundation model for computational pathology," *Nature medicine*, vol. 30, no. 3, pp. 850–862, 2024.

[25] D. Tellez, G. Litjens, P. Bández, W. Bulten, J.-M. Bokhorst, F. Ciompi, and J. van der Laak, "Quantifying the effects of data augmentation and stain color normalization in convolutional neural networks for computational pathology," *Medical Image Analysis*, vol. 58, p. 101544, 2019.

[26] A. L. Moreira, P. S. Ocampo, Y. Xia, H. Zhong, P. A. Russell, Y. Minami, W. A. Cooper, A. Yoshida, L. Bubendorf, M. Papotti, *et al.*, "A grading system for invasive pulmonary adenocarcinoma: a proposal from the international association for the study of lung cancer pathology committee," *Journal of Thoracic Oncology*, vol. 15, no. 10, pp. 1599–1610, 2020.

[27] P. A. Russell, Z. Wainer, G. M. Wright, M. Daniels, M. Conron, and R. A. Williams, "Does lung adenocarcinoma subtype predict patient survival?: A clinicopathologic study based on the new international association for the study of lung cancer/american thoracic society/european respiratory society international multidisciplinary lung adenocarcinoma classification," *Journal of Thoracic Oncology*, vol. 6, no. 9, pp. 1496–1504, 2011.

[28] A. Al-Rubaian, G. N. Gunesli, W. A. Althakfi, A. Azam, D. Snead, N. M. Rajpoot, and S. E. A. Raza, "Cellomaps: A compact representation for robust classification of lung adenocarcinoma growth patterns," *Computers in Biology and Medicine*, vol. 192, p. 110127, 2025.

[29] A. Dosovitskiy, "An image is worth 16x16 words: Transformers for image recognition at scale," *arXiv preprint arXiv:2010.11929*, 2020.

[30] N. L. S. T. R. Team, "Reduced lung-cancer mortality with low-dose computed tomographic screening," *New England Journal of Medicine*, vol. 365, no. 5, pp. 395–409, 2011.

[31] J. Cancer Genome Atlas Research Network *et al.*, "The cancer genome atlas pan-cancer analysis project," *Nat. Genet*, vol. 45, no. 10, pp. 1113–1120, 2013.

[32] A. Vaidya, A. Zhang, G. Jaume, A. H. Song, T. Ding, S. J. Wagner, M. Y. Lu, P. Doucet, H. Robertson, C. Almagro-Perez, *et al.*, "Molecular-driven foundation model for oncologic pathology," *arXiv preprint arXiv:2501.16652*, 2025.

[33] A. Zhang, G. Jaume, A. Vaidya, T. Ding, and F. Mahmood, "Accelerating data processing and benchmarking of ai models for pathology," *arXiv preprint arXiv:2502.06750*, 2025.

[34] M. Heusel, H. Ramsauer, T. Unterthiner, B. Nessler, and S. Hochreiter, "Gans trained by a two time-scale update rule converge to a local nash equilibrium," *Advances in neural information processing systems*, vol. 30, 2017.

[35] J. Deng, W. Dong, R. Socher, L.-J. Li, K. Li, and L. Fei-Fei, "Imagenet: A large-scale hierarchical image database," in *2009 IEEE conference on computer vision and pattern recognition*, pp. 248–255, Ieee, 2009.

[36] B. Wu, C. Xu, X. Dai, A. Wan, P. Zhang, Z. Yan, M. Tomizuka, J. Gonzalez, K. Keutzer, and P. Vajda, "Visual transformers: Token-based image representation and processing for computer vision," 2020.

[37] D. P. Kingma, "Adam: A method for stochastic optimization," *arXiv preprint arXiv:1412.6980*, 2014.

[38] M. Y. Lu, B. Chen, D. F. Williamson, R. J. Chen, I. Liang, T. Ding, G. Jaume, I. Odintsov, L. P. Le, G. Gerber, *et al.*, "A visual-language foundation model for computational pathology," *Nature medicine*, vol. 30, no. 3, pp. 863–874, 2024.